Journal of Trace Elements in Medicine and Biology 52 (2019) 166–175

Contents lists available at ScienceDirect

Journal of Trace Elements in Medicine and Biology

journal homepage: www.elsevier.com/locate/jtemb

µXRF and LA-ICP-TQMS for quantitative bioimaging of iron in organ samples of a hemochromatosis model

Jennifer-Christin Müller[a], Maximilian Horstmann[a], Lisa Traeger[b], Andrea U. Steinbicker[b], Michael Sperling[a,c], Uwe Karst[a,*]

[a] University of Münster, Institute of Inorganic and Analytical Chemistry, Corrensstraße 30, 48149 Münster, Germany
[b] University of Münster, University Hospital Münster, Department of Anesthesiology, Intensive Care and Pain Medicine, Albert-Schweitzer-Campus 1, 48149 Münster, Germany
[c] European Virtual Institute for Speciation Analysis (EVISA), Mendelstraße 11, 48149 Münster, Germany

ARTICLE INFO

Keywords:
Elemental bioimaging
Micro X-ray fluorescence analysis (µXRF)
Laser ablation-inductively coupled plasma-mass spectrometry (LA-ICP-MS)
Triple quadrupole ICP-MS
Hereditary hemochromatosis
Iron overload

ABSTRACT

Hereditary hemochromatosis is the most common autosomal recessive genetic disorder of the iron metabolism. Iron accumulation in various organs, especially in liver and pancreas leads to diseases and may cause organ failure. In this study, methods for elemental bioimaging by means of quantitative micro X-ray fluorescence analysis (µXRF) and laser ablation-inductively coupled plasma-triple quadrupole mass spectrometry (LA-ICP-TQMS) were developed and applied to investigate the pathophysiological development of iron accumulation in murine tissue based on animals with an iron-overload phenotype caused by a hepatocyte-specific genetic mutation. The use of an external calibration with matrix-matched gelatin standards enables the quantification of iron by means of µXRF without the typically used fundamental parameters method or Monte Carlo simulation, which becomes more imprecise when analyzing thin tissue sections. A fast, non-destructive screening of the iron concentration and distribution with a spatial resolution of 25 µm in liver samples of iron-overload mice was developed. For improved limits of detection and higher spatial resolution down to 4 µm, LA-ICP-TQMS was used with oxygen as reaction gas. By monitoring the mass shift of ^{56}Fe to $^{56}Fe^{16}O$, a limit of detection of 0.5 µg/g was obtained. With this method, liver and pancreas samples of iron-overload mice as well as control mice were successfully analyzed. The high spatial resolution enabled the analysis of the iron distribution in different liver lobules. Compared to the established Prussian blue staining, both developed methods proved to be superior due to the possibility of direct iron quantification in the tissues.

1. Introduction

Hereditary hemochromatosis is an autosomal recessive inherited disorder of the iron metabolism characterized by unlimited absorption of iron in the intestine and an accumulation of excess iron in iron storage organs [1,2]. Iron is an essential trace element, which plays an important role in the body. With about 70%, the most common form of iron in the organism is hemoglobin with its important role in oxygen transport and several enzymes. About 30% of the iron is stored in the liver, spleen and muscle tissue as the iron storage form ferritin. Besides this, many other protein-bound forms of iron exist [2,3]. The systemic iron homeostasis is mainly regulated by the hepatic hormone hepcidin [4]. Up to date, there are five known genetic mutations that lead to hereditary hemochromatosis: mutations in the genes involved in regulation of the expression of hepcidin such as HFE, hemojuvelin (HJV) or transferrin receptor 2; mutations in hepcidin transcription itself; or mutations of the iron absorption channel ferroportin FPN [5,6]. If the induction of hepcidin is hindered, iron is accumulated unregulated in various organs, especially in the liver and pancreas [7,8]. Since the bone morphogenetic protein (BMP) type I receptor ALK3 is essential for the hepcidin expression, hepatocyte-specific *Alk3* deficient mice, present with severe iron overload [9]. The BMP receptor ALK2 plays a minor role, as mice with hepatocyte-specific *Alk2* deficiency maintain baseline hepcidin expression, but fail to induce hepcidin in the inflammatory setting [10].

To gain more information about the pathophysiological

Abbreviations: LA-ICP-MS, laser ablation-inductively coupled plasma-mass spectrometry; LOD, limit of detection; LOQ, limit of quantification; µXRF, micro X-ray fluorescence analysis; TQ, triple quadrupole

* Corresponding author.
E-mail address: uk@uni-muenster.de (U. Karst).

https://doi.org/10.1016/j.jtemb.2018.12.012
Received 28 August 2018; Received in revised form 14 December 2018; Accepted 21 December 2018
0946-672X/

development of the iron overload when both receptors are deficient (hepatocyte-specific *Alk2/Alk3* double knock-out), the iron distribution and concentration in various organs of these model animals in comparison to control animals needs to be analyzed. In this paper, two different quantitative elemental bioimaging approaches for the investigation of iron in tissue are presented as advantageous addition to the typically used Prussian blue staining, which can only provide qualitative information about the iron distribution [1].

Elemental bioimaging is an emerging field to analyze the concentration and distribution of essential or toxic metals in the organism or for studying the distribution of drugs in the tissue [11]. Micro-X-ray fluorescence analysis (μXRF) is an elemental imaging approach based on the detection of characteristic secondary X-rays from the material after excitation with high energy X-rays [12]. With this method, a fast and non-destructive analysis of elemental distributions in archeological, geological and biological samples is possible [13–15]. In human liver biopsy samples, μXRF analysis was used to analyze copper with a spatial resolution of 25 μm [15]. In addition to the non-destructive nature of this method, multi-element analysis is possible [16,17]. To obtain quantitative results by means of μXRF, mathematical approaches are typically used. One example for such a mathematical quantification is the fundamental parameters method, in which the physical processes leading to emission of fluorescence radiation are described by analytical equations [18]. Using this method, essential elements in brain tissue were quantified [19]. By using Monte Carlo simulations, variable parameters such as the distance between sample and detector, sample thickness, sample inhomogeneities or different surfaces are better compensated [20]. For example, Padilla *et al.* used a Monte Carlo approach to simulate the radiation transport from the output of the lens to the detector active volume for the quantitative analysis of archaeological pottery samples [21]. However, not exactly approximated parameters may lead to false results. The assumption of infinite thick samples can deliver sufficient results for thick geological samples, but for thin tissue sections, the thickness-dependent analyte fluorescent radiation intensity needs to be taken into account [20]. To overcome those problems, reference standards as similar as possible to the unknown sample can be used [14]. The use of matrix-matched reference materials has been used for the analysis of plant material [22]. Nevertheless, the limit of detection (LOD) of the benchtop μXRF is relatively high compared to other methods, due to the higher penetration depth of the X-rays and thereby increased matrix effects and lower signal-to-noise ratios.

To obtain lower LODs and a higher spatial resolution, laser ablation-inductively coupled plasma-mass spectrometry (LA-ICP-MS) can be used for elemental bioimaging [11]. With this method, laser spot sizes down to 1 μm can be achieved [23]. By using a triple-quadrupole instrument (ICP-TQMS), polyatomic interferences on the analytes of interest can be significantly decreased to improve the LOD even further [24]. The quantification by means of matrix-matched reference standards is much more popular for this method and was previously used for the quantification of copper in liver tissue samples [25,26].

In this paper, a novel quantification approach for μXRF analysis is presented. Matrix-matched gelatin standards were used to quantify the iron distribution in liver tissue of a murine iron-overload model. To the best of our knowledge, there is no benchtop μXRF quantification strategy described for metals in thin tissue samples based on matrix-matched external calibration. To verify the results, comprehensive LA-ICP-TQMS analysis with the same spatial resolution of 25 μm was used for liver, small intestine and pancreas samples. In addition to that, high spatial resolution LA-ICP-TQMS results obtained with a laser spot size of 4 μm are presented. With this resolution, periportal and centrilobular liver lobules can be differentiated, which is needed to analyze the pathophysiological development of the iron overload. The combination of non-destructive quantitative μXRF imaging with high spatial resolution LA-ICP-TQMS imaging is an advantageous addition to the typically used staining procedure and offers new insights into the iron accumulation mechanisms of the hemochromatosis animal model.

2. Materials and methods

2.1. Chemicals

All chemicals were used in the highest quality available. Arsenic ICP standard (1000 mg/l), aluminum sulfate, nitric acid (69%), potassium ferrocyanide trihydrate, ethanol and xylene were obtained from Merck (Darmstadt, Germany). Iron(II) sulfate heptahydrate and hydrochloric acid (37%) were purchased from VWR Chemicals (Haasrode, Belgium). Gelatin was obtained from Grüssing (Filsum, Germany). Doubly distilled water was freshly prepared daily using an Aquatron Water Still purification system model A400D (Barloworld Scientific, Nemours Cedex, France).

2.2. Animal study

The study was carried out in accordance with the recommendations and approval of the institutional ethics committee of the North Rhine-Westphalian Agency for Nature, Environment, and Consumer Protection (permit no. Az.84-02.05.2012.181). Mice with homozygous *loxP*-flanked ("floxed") *Alk2* (*Alk2*$^{fl/fl}$) [27,28] and *Alk3* alleles (*Alk3*$^{fl/fl}$) [27–29] on a C57BL/6 background were bred with B6.Cg-Tg$^{(Alb-Cre)21Mgn}$/J mice to obtain homozygous animals (*Alk2/3*$^{fl/fl}$) with and without a *Cre* recombinase driven by the hepatocyte-specific albumin promoter. Mice were held in individually ventilated cages and fed a standard diet with an iron content of 198 μg/g (Altromin Spezialfutter GmbH & Co. KG, Lage, Germany). Twelve-week-old male mice with hepatocyte-specific *Alk2* and *Alk3* (*Alk2/3*$^{fl/fl}$; *Alb-cre*) deficiency and control mice (*Alk2/3*$^{fl/fl}$) were included in this study.

2.3. Sample preparation

Tissue samples were harvested and incubated in 4% paraformaldehyde overnight. Liver, small intestine and pancreas samples were embedded in paraffin and cut into 5 μm thin sections using a rotary microtome Autocut 1140 (Reichert-Jung, Wetzlar, Germany) with Feather Typ S35 stainless steel blades. Afterwards, the thin sections were mounted on Starfrost® microscope slides (Engelbrecht, Edermünde, Germany) at the Institute of Neuropathology at the University Hospital in Münster. Prior to the analysis, the sample sections were deparaffinized and rehydrated (10 min xylene, 2 min 100% ethanol, 2 min 90% ethanol, 2 min 70% ethanol, 2 min bidest. H_2O). Bright field microscopic images of the unstained tissue samples were captured with a BZ-9000 microscope (Keyence, Osaka, Japan).

2.4. Prussian blue staining and tissue iron content

Prussian blue staining on paraffin-embedded tissue samples was used to detect non-heme iron accumulation. Tissue sections were incubated in 5% potassium ferrocyanide trihydrate with 5% hydrochloric acid for 15 min and washed with aqua bidest H_2O. Microscopic images of the stained samples were obtained with the same microscope as described for unstained samples.

Non-heme tissue iron content was determined in duplicates using the assay protocol described by Torrance and Bothwell [30]. Tissue samples digested in 100 μl acid (3 M hydrochloric acid, 0.61 M trichloracetic acid at 65 °C and 550 rpm for three days) as well as standard solutions were incubated with 50 μl chromagen solution (one part chromagen stock solution containing 1.86 mM bathophenantroline sulfonate, 143 mM thioglycolic acid, one part saturated sodium acetate solution and five parts of water) for 10 min at room temperature in the dark. Samples were diluted with the same acid solution used for digestion of the tissue and the absorbance at 540 nm was determined with a BioTek plate reader.

2.5. Preparation of matrix-matched standards

For quantification, an external calibration with matrix-matched gelatin standards was performed. Gelatin (10% w/w) was spiked with aqueous solutions of iron(II) sulfate heptahydrate in a concentration range from 0 up to approx. 30 mg/g. The gelatin mixture was homogenized at 37 °C and 5 µm thin sections, according to the thickness of the samples, were prepared using a cryomicrotome (CryoStar NX70, Thermo Scientific, Waltham, MA, USA). The standard sections were mounted on the same microscope slides as the samples to reduce variations in background intensities. Especially for µXRF measurements, those differences may change the results, because of the relatively high penetration depth of the X-ray beam.

For µXRF analysis, a region of (1 × 1) mm of each standard was scanned with the same setup as for the sample. For LA-ICP-TQMS analysis, ten lines with 50 data points per line were recorded for each standard. The averaged intensities were then used to calculate a calibration curve for both methods.

2.6. Bulk analysis of matrix-matched standards

Bulk analysis after digestion with nitric acid was used to validate the iron concentration in the gelatin standards. Exactly 100 mg standard was digested with 1 ml conc. nitric acid and then diluted with bidest. H_2O to concentrations around 10 µg/g. 100 µl of this solution was mixed with the same amount of arsenic (10 µg/g in 20% HNO_3, diluted from 1000 µg/g ICP standard). Since arsenic has a characteristic emission line near the emission line of iron without overlapping of the signals and in addition to that, no background signal of arsenic was detected in the tissue samples, this element can be used as internal standard. Aliquots of 5 µl were dried onto quartz glass discs (Bruker Nano, Berlin, Germany) for total-reflection X-ray fluorescence analysis (S2 Picofox, Bruker Nano). The instrument was equipped with a molybdenum X-ray tube, which was operated at a power of 37.5 W (750 µA, 50 kV). An energy-dispersive, Peltier-cooled silicon drift-detector (SDD, XFlash) was used and the analysis time per sample was set to 500 s. For data evaluation, the software Spectra Picofox Version 7.2.5.0 (Bruker Nano) was used.

2.7. µXRF analysis

For µXRF analysis, the M4 Tornado (Bruker Nano) with the Esprit Software (Version 1.2) was used. The system was equipped with a Rh X-ray tube, which was operated at 30 W (50 kV, 600 µA). To minimize interferences with elements in the air, the analyses were carried out at a reduced pressure of 20 mbar. To find the best compromise between analysis time, signal-to-noise ratio and standard deviation in the standards, the number of scan cycles as well as the analysis time per pixel, were variated. The fastest analysis with the lowest standard deviation for each standard was achieved with a single scan and analysis time of 100 ms per pixel. Those parameters were used for all further analysis. The distance between the spots was set to 25 µm, to ensure a complete scan of the sample with the approximately 25 µm large X-ray spot of the instrument.

2.8. LA-ICP-TQMS analysis

The LA-ICP-TQMS analysis was carried out with an iCAP TQ instrument (Thermo Fisher Scientific, Bremen, Germany) coupled to a LSX213 G2$^+$ laser ablation system (Teledyne CETAC Technologies, Omaha, NE, USA). The laser ablation system was equipped with a Nd:YAG laser with a wavelength of 213 nm. The shot frequency was set to 20 Hz and laser spot sizes of 25 and 4 µm were chosen with scan speeds of 50 and 8 µm/s for line-wise ablation. The laser energy was adjusted for samples and standards individually to ensure complete ablation of the material. The HelEx Active 2-Volume cell (Teledyne CETAC Technologies) was flushed with a helium gas flow of 0.8 l/min. For plasma stability, an additional argon gas flow (˜0.9 l/min, daily tuned) was added after the cell with a T-piece. The ablated aerosol was transported into the ICP-MS via Tygon® tubing. For sample introduction into the plasma, a quartz injector pipe with an inner diameter of 3.5 mm was used. The ICP-MS was equipped with nickel sampler and skimmer cones. The torch position and lens voltages were tuned daily with respect to best sensitivity. To reduce polyatomic interferences, the ICP-MS was operated in the triple quadrupole mode with oxygen as reaction gas (0.39 ml/min). The intensities of the isotopes ^{31}P, ^{32}S, ^{54}Fe, ^{56}Fe and ^{57}Fe were recorded as their corresponding ^{16}O cluster ions with dwell times of 100 ms each. The following ICP-MS parameters were used: rf power 1550 W, cool gas flow 14 l/min, auxiliary gas flow 0.8 l/min.

2.9. Data evaluation

The µXRF raw data sets were converted into *csv* files using an in-house developed software, which allows to extract the data of the corresponding channels for each element of interest. For each element, a range of ± 15 kV was selected. To determine calibration curves from the µXRF data, the converted data sets were evaluated using Microsoft Excel 2016® (Microsoft Corporation, Redmond, WA, USA). The *csv* files of the samples as well as the LA-ICP-TQMS data sets were converted into 2D images with another in-house developed software.

3. Results and discussion

3.1. Non-heme tissue iron content

To analyze the total non-heme tissue iron content of the samples, tissue was digested and the absorbance after complex formation with bathophenantroline sulfonate was determined. Table 1 summarizes the results for the investigated liver samples. Due to the small size of the pancreas and its utilization for imaging analysis, no quantification of the bulk iron content could be performed of these samples.

The hepatocyte-specific *Alk2/3* deficient animals (*Alk2/3*$^{fl/fl}$; *Alb-cre, animals with expression of the Cre recombinase driven by the hepatocyte-specific albumin promoter)* that present with severe iron overload showed significantly increased iron concentrations around 1500 µg/g in the liver, whereas the iron concentration in the liver of control animals (*Alk2/3*$^{fl/fl}$, floxed animals without expression of the Cre recombinase) was below 200 µg/g. These values correlate well with the normal levels for iron in the liver of mice, which has been described to be approx. 150 µg/g [32]. The differentiation between the hepatocyte-specific *Alk2/3* deficient and control animals was easily possible, but a relatively high biological variation between the analyzed samples of one genotype can be observed. For example, the iron concentration of sample 1d was approx. 1.9 times higher than the iron concentration found for sample 1a. The same biological variation can be found for the two control samples. However, the differentiation of control and *Alk2/3* deficient animals is easily possible despite the high biological variations since the diseased animals have an approximately 12 times higher iron content found in the liver. To obtain more information about the

Table 1
Overview of analyzed samples with genotype [31] and determined non-heme liver iron content.

Sample ID	Genotype	c(Fe)/ µg·g^{-1}
Sample 1a	*Alk2/3*$^{fl/fl}$; *Alb-cre* (*Alk2/3* deficient)	1098
Sample 1b	*Alk2/3*$^{fl/fl}$; *Alb-cre* (*Alk2/3* deficient)	1491
Sample 1c	*Alk2/3*$^{fl/fl}$; *Alb-cre* (*Alk2/3* deficient)	1409
Sample 1d	*Alk2/3*$^{fl/fl}$; *Alb-cre* (*Alk2/3* deficient)	2076
Sample 2a	*Alk2/3*$^{fl/fl}$ (control)	51
Sample 2b	*Alk3*$^{fl/fl}$ (control)	196

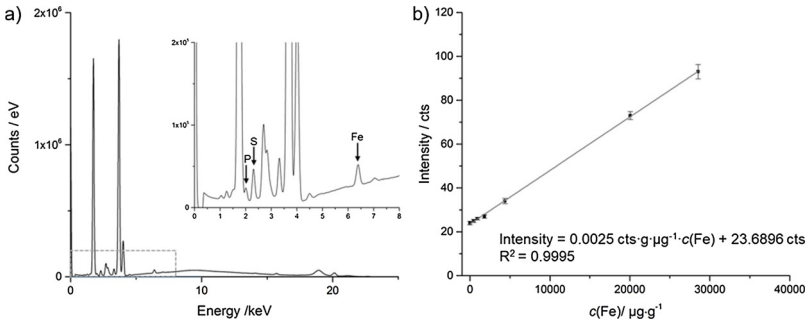

Fig. 1. a) µXRF sum spectrum of liver sample 1a with enlarged section of the region of interest and labels for the fluorescence peaks of phosphorous, sulfur and iron, b) µXRF calibration curve of iron for matrix-matched gelatin standards with calibration function and standard deviations.

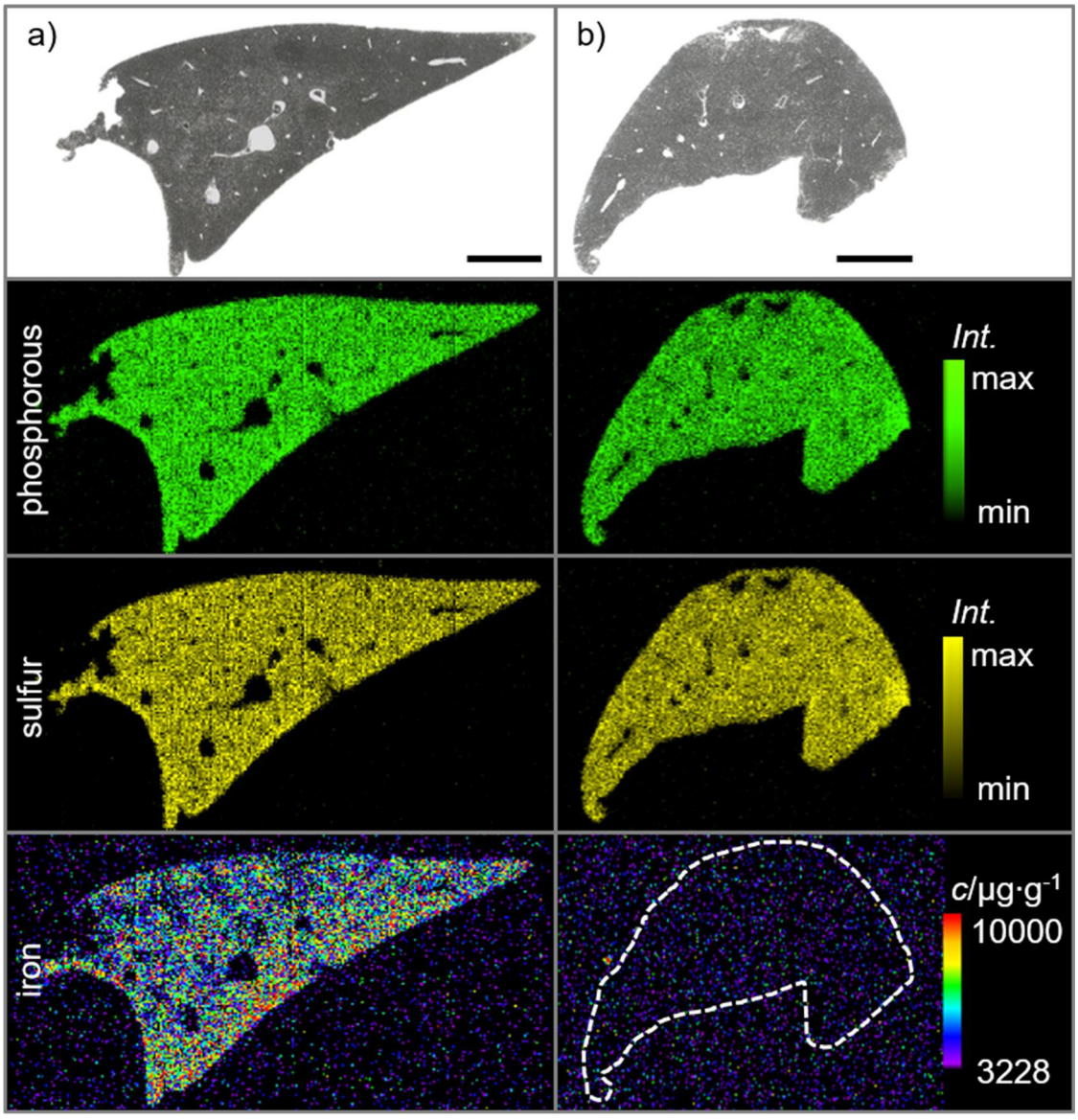

Fig. 2. Microscopic images (upper row) and µXRF data of the qualitative elemental distributions of phosphorous (green) and sulfur (yellow) as well as the quantitative iron distribution for a) hepatocyte-specific Alk2/3 deficient liver sample 1a and b) control liver sample 2a. The black scale bar indicates 1 mm. (For interpretation of the references to colour in this figure legend, the reader is referred to the web version of this article).

pathophysiological development of the iron overload in the liver and in other organs, quantitative bioimaging methods were applied in a next step in addition to the established staining procedures, since the bulk analysis is not able to account for inhomogeneous iron distributions in the liver or pancreas.

3.2. Quantitative bioimaging by means of μXRF

Since benchtop μXRF is a non-destructive and fast method, which requires only minimal sample preparation, an easy quantification approach was developed to analyze the elemental distribution in the tissue samples. In Fig. 1a, the sum spectra for the liver of the hepatocyte-specific *Alk2/3* deficient sample 1a are shown. The K_α emission lines, caused by an electron transition from the 2p orbital (L shell) to the 1 s orbital (K shell), were observed due to the high intensity of these lines for the analyzed elements. The signal of the $K_{\alpha1}$ emission line of phosphorous at 2.01 keV showed a slight overlap with the high signal from the $K_{\alpha1}$ signal of silicon (1.74 keV) from the microscopic glass slide. In contrast to that, the sulfur $K_{\alpha1}$ signal at 2.31 keV was higher and better separated than the phosphorous signal. Both elements could be used to visualize the tissue, due to the endogenous occurrence of phosphorous and sulfur in for example amino acids or phospholipids. The $K_{\alpha1}$ emission line of iron has an energy of 6.4 keV. In this region, the background signal is increased due to the Bremsstrahlung of the X-ray tube. Thus, the signal-to-noise ratio for iron is not as high as for sulfur, which adversely affects the LOD.

To determine the LOD for iron by means of μXRF, an external matrix-matched calibration was performed. The calibration curve for iron in gelatin standards is shown in Fig. 1b. The actual concentrations after bulk analysis of the standards are used for generation of the calibration curve. With those values, a good linearity over a wide concentration range could be observed with a coefficient of determination of $R^2 = 0.9995$ over all calibration points. Even with an iron concentration of approx. 30 mg/g in the highest matrix-matched standard, the linear dynamic range of the detector was not reached, since no decrease of the slope of the calibration curve can be observed. The standard deviation between the 40 analyzed lines for each concentration was calculated and was sufficiently low for all matrix-matched standards with values under 5%, as shown in Fig. 1b. In contrast to ICP-MS, for which the torch and lens settings are tuned daily to obtain the best signal intensities, the settings of the X-ray tube are constant. Thus, the day-to-day variation between the obtained calibration curves was below 2%, even when the X-ray tube was turned off between the measurements. Therefore, a daily external calibration of the μXRF was not required. This leads to an overall shorter analysis time compared to LA-ICP-TQMS analysis.

The low slope of the calibration curves indicated that the sensitivity of the method is relatively low (Fig. 1b). In addition to that, the LOD and LOQ, calculated according to Boumans [33], were 970 μg/g and 3230 μg/g, respectively, for iron in a 5 μm thin tissue section. This can be explained by the elevated background signal for iron caused by the Bremsstrahlung in the energy region of the iron $K_{\alpha1}$ emission line.

In Fig. 2a, the phosphorous, sulfur and iron distributions of the hepatocyte-specific *Alk2/3* deficient liver sample 1a are shown. The distribution maps of phosphorous and sulfur showed a very homogenous distribution without variations in the tissue density. In this setting, the blood vessels and bile ducts in the liver sample can be identified. Hence, the tissue can be easily visualized with μXRF. The lower limit of the concentration scale for the iron distribution was set to the LOQ to remove the background signal. Iron concentrations up to 10 mg/g were found with a relatively inhomogeneous distribution in the tissue of the hepatocyte-specific *Alk2/3* deficient liver. Highest concentrations were observed at the lower sample edge, whereas lower concentrations were located in the upper region of this liver section. Nevertheless, despite the high LOD, the iron concentrations for the hepatocyte-specific *Alk2/3* deficient liver sample were high enough to be quantified with the developed method.

In addition to the successful quantification of high iron concentrations, the developed μXRF method allowed the analysis of paraffin-embedded as well as deparaffinized tissue samples. For LA-ICP-TQMS analysis, paraffin had to be removed because the spatial resolution is destroyed when the embedding medium melts during ablation. For μXRF analysis, this effect should be irrelevant and therefore, a comparison of the same sample with and without paraffin was possible. The average iron concentration in the tissue was less than 5% lower after the deparaffinization process, and the distribution appeared to be almost identical (images not shown here). These results indicate that the analysis of paraffin-embedded samples is also possible. This minimizes the sample preparation time and can be an advantage for the investigation of water-soluble analytes.

Despite the positive results for the hepatocyte-specific *Alk2/3* deficient sample, the quantitative μXRF approach also has some limitations. In Fig. 2b, the phosphorous, sulfur and iron distributions for the liver of the control animal are shown. Again, the tissue could be visualized using the endogenous elements phosphorous and sulfur, but the iron distribution was not distinguishable from the background signal. As expected from the bulk iron analysis, the iron concentration for this animal was much lower than the concentration found for the hepatocyte-specific *Alk2/3* deficient sample and lower than the LOD of the μXRF method. To determine the iron concentration and distribution in control animals, a more sensitive method was needed.

3.3. Quantitative bioimaging by means of LA-ICP-TQMS

LA-ICP-TQMS was selected as more sensitive method for the analysis of iron-overload as well as control tissue samples. With this established elemental bioimaging method, the results from the μXRF analysis could be verified. Due to many polyatomic interferences (e.g. $^{40}Ar^{16}O^+$, $^{40}Ca^{16}O^+$, $^{40}Ar^{15}N^1H^+$, $^{38}Ar^{18}O^+$, $^{38}Ar^{17}O^1H^+$) [34], especially affecting the most abundant iron isotope ^{56}Fe (rel. abundance 91.75%), the triple quadrupole mode with oxygen as reaction gas was used. Again, matrix-matched gelatin standards were used to simulate the tissue matrix with respect to potential matrix effects influencing the ablation and atomization behavior. A laser spot size of 25 μm was applied to obtain a spatial resolution comparable to μXRF analysis. The external calibration showed low relative standard deviations between the ablated lines of 6% and lower, as well as a good linearity of $R^2 = 0.9989$ and better over the wide concentration range. LOD and LOQ for ^{56}Fe as $^{56}Fe^{16}O$ of 0.5 μg/g and 1.5 μg/g, respectively, were obtained. With this superior LOD compared to μXRF analysis (LOD 970 μg/g), the same liver tissue sections were analyzed. Since the isotope ^{56}Fe had the lowest LOD compared to the two other analyzed isotopes (5.7 μg/g for ^{54}Fe and 2.1 μg/g for ^{57}Fe), only the results for ^{56}Fe are presented in the following. However, the obtained images for the other isotopes showed identical iron concentrations and distributions. The LA-ICP-TQMS results for the hepatocyte-specific *Alk2/3* deficient and control liver samples 1a and 2a are shown in Fig. 3. Again, the sulfur and phosphorous distributions could be used to visualize the tissue structure and for monitoring of the plasma stability. The use of the TQ-O_2 mode was inevitable when analyzing sulfur by means of ICP-MS, because of interferences with dimeric oxygen species.

As already observed with μXRF, the tissue samples were homogeneous without significant variations in the tissue density. For the hepatocyte-specific *Alk2/3* deficient animal, the same concentration scale as for the μXRF results was used. The iron concentration determined with LA-ICP-TQMS was lower compared to the μXRF results, which could be explained with a decrease of possible interferences when using the LA-ICP-TQMS method. Moreover, the higher sensitivity of LA-ICP-TQMS compared to μXRF caused better contrasts in the tissue. Therefore, the inhomogeneous iron distribution especially in the upper part of the tissue could be better visualized with LA-ICP-TQMS.

Another advantage of the significantly improved LOD of the LA-ICP-TQMS method is the possibility to analyze control samples that contain substantially lower levels of iron. The iron concentration of sample 2a could not be analyzed using μXRF (compare Fig. 2b) due to the high LOD. With LA-ICP-TQMS, in contrast, iron concentrations up to 500 μg/g were found (Fig. 3b). With an average tissue concentration of 60 μg/g, the iron values found in the analyzed thin section were in good

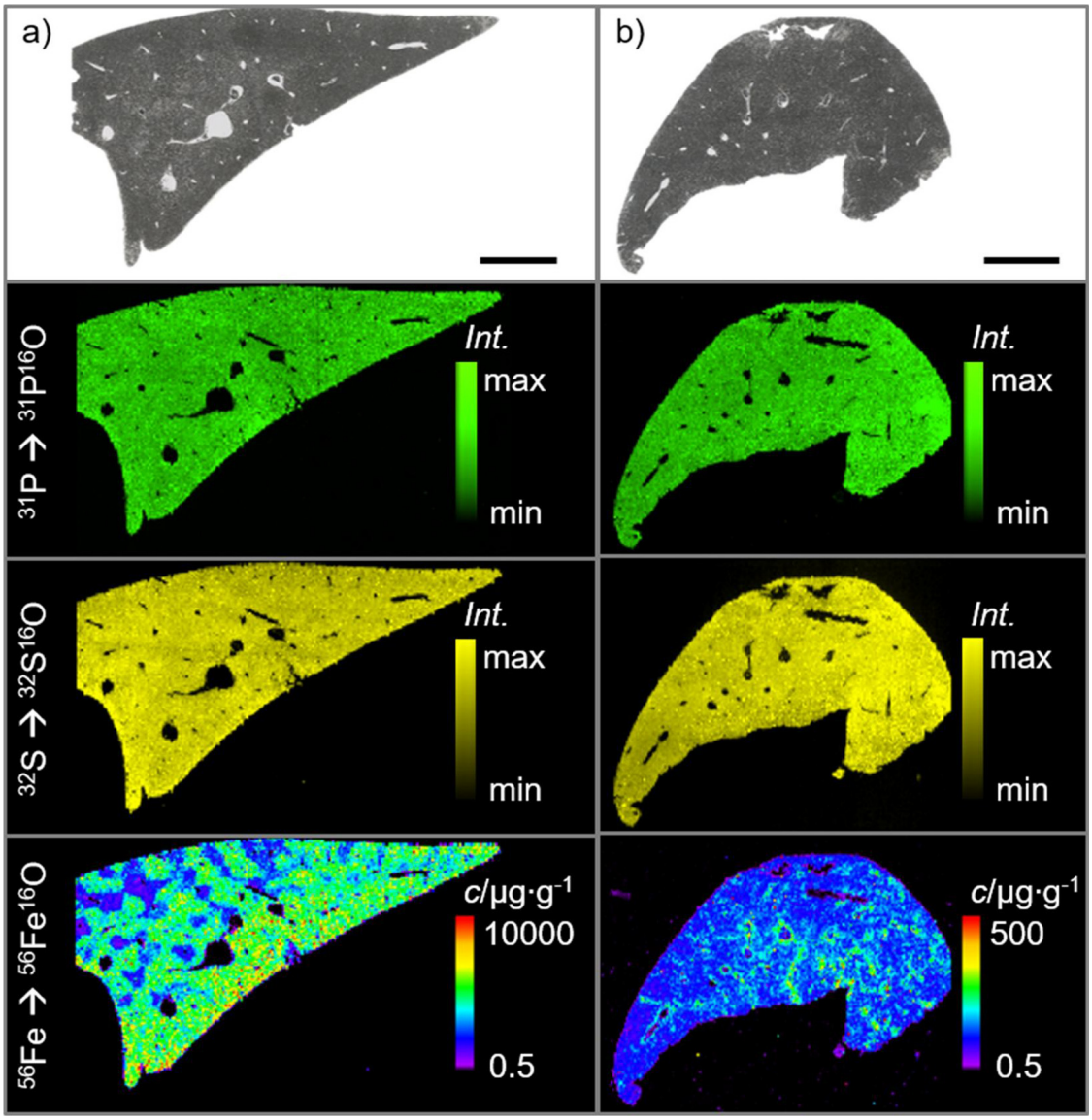

Fig. 3. LA-ICP-TQMS results obtained with a laser spot size of 25 µm for a) hepatocyte-specific Alk2/3 deficient liver sample 1a and b) control liver sample 2a. The black scale bar indicates 1 mm.

accordance with the bulk iron concentration determined in the liver (compare Table 1). Again, the iron distribution was not homogeneous. The highest concentrations in control samples were found directly around the blood vessels and could be traced back to blood depositions. Comparing the LA-ICP-TQMS results for both samples, the iron concentration of hepatocyte-specific *Alk2/3* deficient animals was around 70 times higher than for the control tissue.

To further investigate the iron distribution in the murine model of hereditary hemochromatosis, the small intestine and pancreas samples of control and hepatocyte-specific *Alk2/3* deficient animals were analyzed. Since the pancreas is also affected by iron accumulation in hereditary hemochromatosis, high iron concentrations were expected in this tissue. With µXRF, the iron distribution in the pancreas was visualized, but the intestine region of the tissue section could not be analyzed due to the high LOD. Thus, only LA-ICP-TQMS was used for these tissue samples. The phosphorous, sulfur and iron distribution of the intestine and pancreas of hepatocyte-specific *Alk2/3* deficient animal 1a and control animal 2a obtained with a laser spot size of 25 µm are shown in Fig. 4. The phosphorous and sulfur distributions could be used to visualize the structure of the intestine and the pancreas, which is divided in many small lobules.

For the hepatocyte-specific *Alk2/3* deficient animal, iron concentrations up to 5000 µg/g were found almost exclusively in the pancreas. Only the outer part of the intestinal wall showed slightly increased iron levels. The average concentration in the intestine region was only 496 µg/g compared to an average iron concentration in the pancreas of 1608 µg/g. This shows that the developed LA-ICP-TQMS method can be used to analyze the significant extrahepatic iron overloading in the pancreas as well. The iron concentration found in the pancreas of the control sample was much lower compared to the hepatocyte-specific *Alk2/3* deficient sample with an average iron concentration of 284 µg/g. Interestingly, the iron concentration in the intestine was significantly higher with an average of 776 µg/g. In addition, the iron in the control intestine was primarily found in the circular folds. In an intact iron homeostasis, the distribution of iron from the enterocytes into the circulation is blocked, if the iron supply is sufficient. Hepcidin is secreted and leads to an internalization and degradation of the sole known iron exporter ferroportin. On the other hand, through the regular renewal of the enterocytes, excess iron is excreted [2,8]. Because of this mechanism, the observed iron distribution can be expected for control mice. In contrast to that, the iron uptake from enterocytes into the circulation is not blocked in hepatocyte-

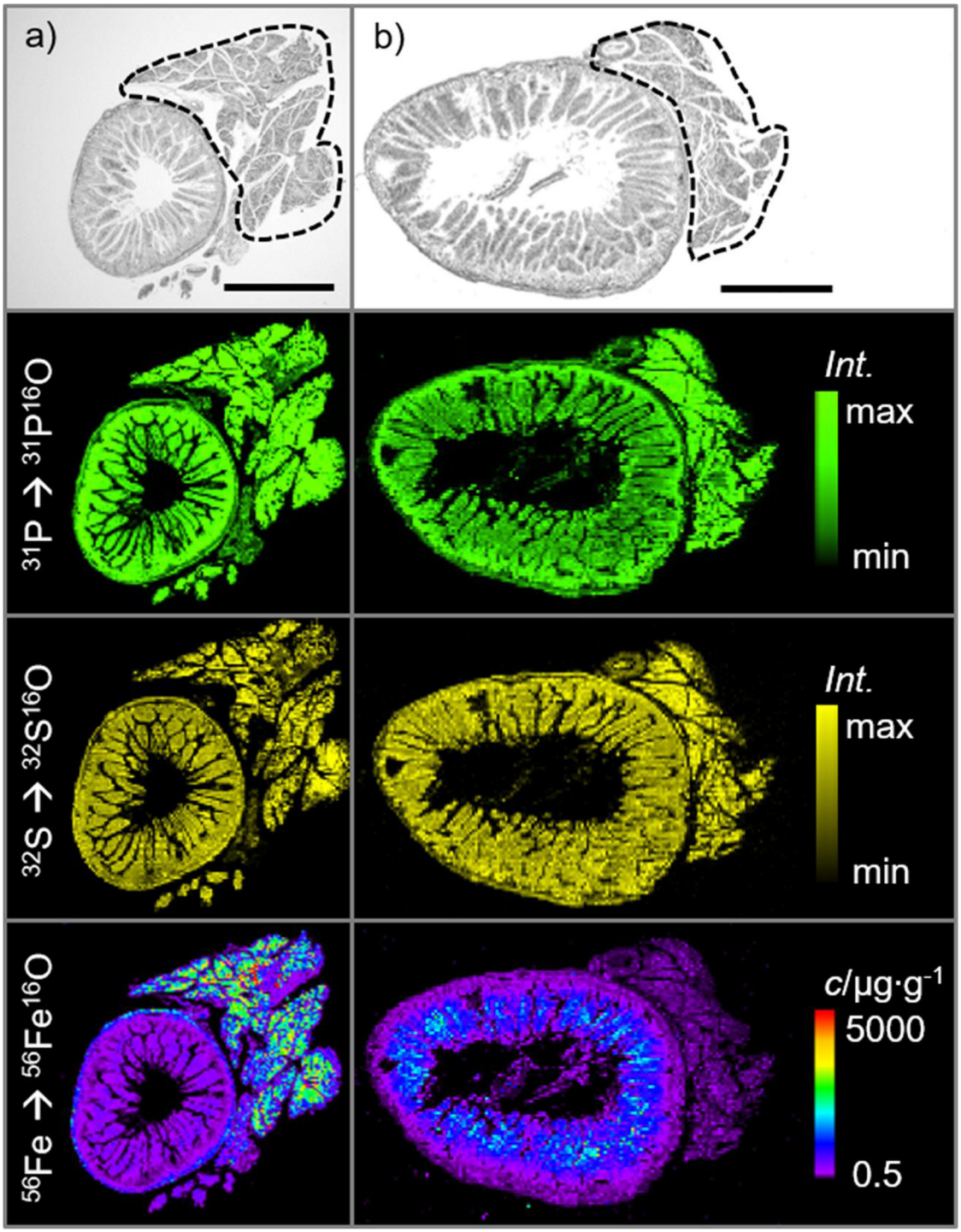

Fig. 4. Bright field microscopic image (upper row), and phosphorous (green), sulfur (yellow) and quantitative iron distribution (LA-ICP-TQMS, 25 µm laser spot size) of the intestine and pancreas of a) the hepatocyte-specific Alk2/3 deficient sample 1a and b) the control sample 2a. The pancreas is marked with a black dotted line; the scale bar indicates 1 mm. (For interpretation of the references to colour in this figure legend, the reader is referred to the web version of this article).

specific *Alk2/3* deficient animals, which leads to lower iron concentrations inside the intestine.

To conclude, the developed LA-ICP-TQMS method is a useful tool to analyze the iron distribution and concentration in the liver, pancreas and intestine of an iron overloaded phenotype as well as in non-overloaded, control tissue. Significant iron overload was detected for hepatocyte-specific *Alk2/3* deficient liver and pancreas samples, whereas the iron concentration in the intestine was slightly reduced compared to control samples.

3.4. High spatial resolution imaging

The structural organization of the liver can be described by the hepatic lobule model. In a hexagonal region around the central vein, portal triads, composed of the portal vein, hepatic artery and bile ducts, are located. Thus, the hepatic parenchyma can be divided into the centrilobular region close to the central vein and the periportal region near the portal triads. Oxygen and nutrition-rich blood enters the liver through the portal vein before draining via the central vein [35]. To further analyze the pathophysiological development of the iron

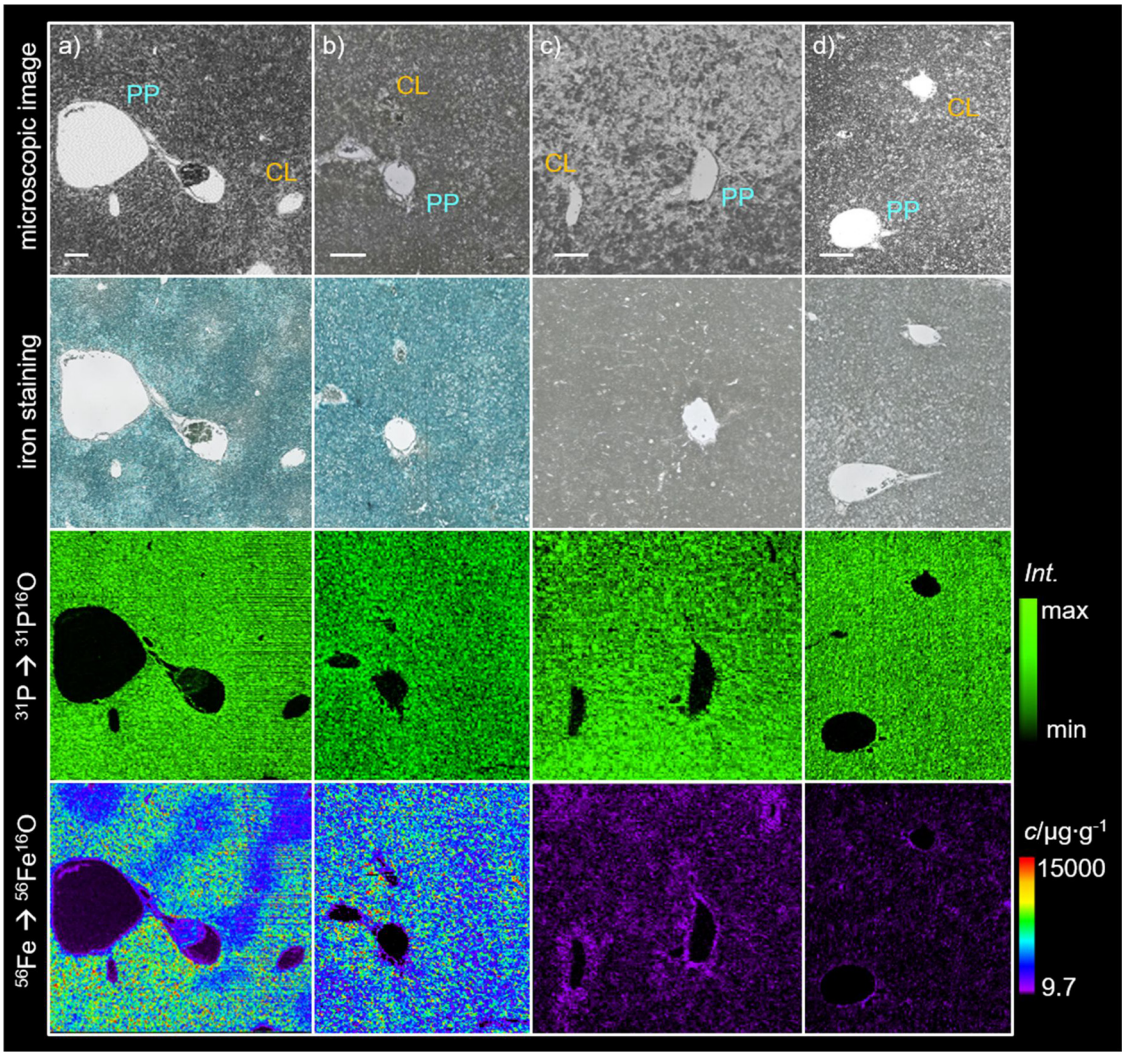

Fig. 5. Bright field microscopic images (upper row), Prussian blue staining (second row) and high spatial resolution LA-ICP-TQMS data (4 µm spot size) of phosphorous (third row) and iron (lower row) of the liver of a) hepatocyte-specific Alk2/3 deficient sample 1a, b) hepatocyte-specific Alk2/3 deficient sample 1b, c) control sample 2a and d) control sample 2b. The scale bar indicates 100 µm; the periportal (PP) and centrilobular (CL) regions are labeled. (For interpretation of the references to colour in this figure legend, the reader is referred to the web version of this article).

accumulation phenotype in the liver of hepatocyte-specific *Alk2/3* deficient animals, the periportal and centrilobular regions need to be differentiated. Different iron-overload animal models present a distinct hepatic iron accumulation pattern in the centrilobular, periportal, or both areas [6,36]. To distinguish the periportal lobules from the centrilobular regions, small parts of the liver samples were analyzed with a higher spatial resolution of 4 µm. The ablated areas were chosen after µXRF analysis, where regions of interest were defined. Because the ablated sample volume per shot on the 5 µm thin tissue with the spatial resolution of 4 µm was only 80 fL, the low LOD realized with the TQ-O_2 mode was necessary. The LOD of $^{56}Fe^{16}O$ determined with a 4 µm spot size was 9.7 µg/g compared to an LOD of 158 µg/g for ^{57}Fe in the single quadrupole kinetic energy discrimination (SQ-KED) mode. Moreover, the sensitivity in the TQ-O_2 mode was 14 times higher than in the SQ-KED mode (slope of the calibration curve: 2.8 cps·g·µg^{-1} and 0.2 cps·g·µg^{-1}, respectively). The results for the high spatial resolution imaging are shown in Fig. 5. The three vessels in the periportal region and the single vessel in the centrilobular region could be easily assigned in the microscopic image. The images of the Prussian blue stained hepatocyte-specific *Alk2/3* deficient samples (Fig. 5a and b) showed a bright blue color, indicating the formation of the iron(III) ferrocyanide complex. The iron distribution of sample 1a seemed to be more inhomogeneous compared to the distribution found for sample 1b. In contrast to that, the images of the control samples after staining showed no indication for the formation of the blue complex. Similar to the µXRF results, the LOD of the Prussian blue staining method was not sufficient to detect iron in the control samples. Moreover, the staining led to only qualitative information. Differences in the blue color brightness could be caused by different iron concentrations in the tissue, but they may also be caused by variations in the complex agent distribution. Therefore, LA-ICP-TQMS with a high spatial resolution of 4 µm is a useful tool for the determination of the iron distribution and concentration in the liver tissue (Fig. 5, lower two rows). As it can be seen in the phosphorous distribution, the spatial resolution of 4 µm is required to sufficiently differentiate between the periportal and centrilobular liver region. For all four samples shown here, the phosphorous distribution was very homogeneous and no variations in the tissue density was observed. As it was expected from the Prussian blue staining, the iron distribution for sample 1a was relatively inhomogeneous compared to sample 1b. The comparison between the stained sample and the LA-ICP-TQMS results were in good accordance, especially with respect to the fact, that parallel slices were used for both methods. As the staining is performed with an iron salt and LA-ICP-TQMS cannot differentiate between iron(II) and iron(III), the stained samples cannot be used for

LA-ICP-TQMS. Nevertheless, both parallel sections of sample 1a showed the highest iron concentrations in both, the periportal and centrilobular region. This result showed that there were only minor differences between non-heme iron (visualized by Prussian blue staining) and total iron (determined by means of LA-ICP-TQMS). Therefore, the developed LA-ICP-TQMS method can be used to complement the established procedures for tissue iron determination. With LA-ICP-TQMS, iron concentrations up to 15,000 µg/g were found. This increase of the maximum concentration compared with the LA-ICP-TQMS analysis with a laser spot size of 25 µm could be explained with less averaging over the iron hotspots when a smaller spot size is used. For sample 1b, the iron concentration was in the same range with a more homogenous distribution in the whole tissue section. When comparing the staining results, sample 1b seemed to have higher iron concentrations compared to sample 1a, due to the more consistent blue color in the tissue. However, the concentrations determined by means of LA-ICP-TQMS show, that sample 1b has a slightly lower iron concentration of around 5380 µg/g compared to an average concentration of 5770 µg/g found for sample1a. Since only small sections of thin tissue slices were analyzed with the laser spot size of 4 µm, these values cannot represent the bulk iron concentration in the liver. However, the comparison indicates, that the optical impression of the stained samples could be misleading regarding the actual concentration, but the iron distribution observed after the staining was in good agreement with the LA-ICP-TQMS results.

In contrast to the hepatocyte-specific *Alk2/3* deficient samples, the iron distribution in the control samples were much lower, as expected from the negative staining results. Nevertheless, with LA-ICP-TQMS, the iron distribution primary around the blood vessels can be visualized. Here, average concentrations of 186 µg/g and 114 µg/g for the samples 2a and 2b, respectively, were found. Again, the significantly better LOD of the LA-ICP-TQMS method compared to the staining procedure led to more detailed information about the quantitative iron distribution in the tissue, especially regarding the control sample.

4. Conclusion

To conclude, both developed methods for quantitative elemental bioimaging present an advantageous addition to the established staining procedures. We were able to analyze the iron concentration and distribution in liver tissue samples of hepatocyte-specific *Alk2/3* deficient mice by using a novel quantification approach for µXRF analysis. By means of external calibration with matrix-matched gelatin standards, the iron overload in hepatocyte-specific *Alk2/3* deficient mice was successfully analyzed. The phosphorous and sulfur distribution can be used to visualize the tissue. For iron, a LOD of 968 µg/g was found, which was sufficient to analyze the iron-overload phenotypes but not the control samples. To obtain a better LOD and to verify the µXRF results, LA-ICP-TQMS with a laser spot size of 25 µm was used in the triple quadrupole mode with oxygen as reaction gas. With this method, polyatomic interferences, especially on the main iron isotope, were significantly reduced, so that a LOD of 0.5 µg/g for iron was achieved. In addition, the phosphorous and sulfur distributions could be used for tissue visualization again. The comparison of both methods shows a slightly lower iron concentration determined by LA-ICP-TQMS, which can be explained with reduced interferences. However, due to the non-destructive scanning, minimal sample preparation without the requirement for deparaffinization and no need for daily calibration, µXRF can be used as quantitative pre-screening method. Especially the fast analysis and the lower acquisition and operating costs are an advantage of the developed µXRF method compared to LA-ICP-TQMS analysis.

In addition to the liver samples, small intestine and pancreas samples of hepatocyte-specific *Alk2/3* deficient mice as well as control samples were successfully analyzed with LA-ICP-TQMS. As expected, the iron concentration in the liver and pancreas of hepatocyte-specific *Alk2/3* deficient animals were much higher than for the control animals. However, the iron concentration in the small intestine was slightly higher for control phenotypes, due to the reduced uptake of iron into the organism.

Moreover, LA-ICP-TQMS enabled high spatial resolution analysis with a laser spot size of 4 µm. With this resolution, the periportal and centrilobular liver regions could be differentiated. The complementary use of staining techniques, quantitative µXRF analysis and LA-ICP-TQMS allows to combine the advantages and overcome the challenges of each method and can lead to new insights in the development of iron accumulation in hereditary hemochromatosis.

Conflict of interest

All authors declare that there are no conflicts of interest associated with this manuscript.

Acknowledgements

The authors would like to thank Michael Kießhauer and Robin Schmid for the development of and the support with the µXRF- and imaging software.

References

[1] A. Pietrangelo, Hereditary hemochromatosis: pathogenesis, diagnosis, and treatment, Gastroenterology 139 (2010) 393–408, https://doi.org/10.1053/j.gastro.2010.06.013.
[2] A. Reuben, J.W. Chung, R. Lapointe, M.M. Santos, The hemochromatosis protein HFE 20 years later: an emerging role in antigen presentation and in the immune system, Immun. Inflamm. Dis. 5 (2017) 218–232, https://doi.org/10.1002/iid3.158.
[3] I. Milto, I. Suhodolo, V. Prokopieva, T. Klimenteva, Molecular and cellular bases of iron metabolism in humans, Biochemistry 81 (2016) 725–742, https://doi.org/10.1134/S0006297916060018.
[4] A.U. Steinbicker, M.U. Muckenthaler, Out of balance-systemic iron homeostasis in iron-related disorders, Nutrients 5 (2013) 3034–3061, https://doi.org/10.3390/nu5083034.
[5] D.F. Wallace, L. Summerville, E.M. Crampton, D.M. Frazer, G.J. Anderson, V.N. Subramaniam, Combined deletion of Hfe and transferrin receptor 2 in mice leads to marked dysregulation of hepcidin and iron overload, Hepatology 50 (2009) 1992–2000, https://doi.org/10.1002/hep.23198.
[6] A.U. Steinbicker, T.B. Bartnikas, L.K. Lohmeyer, P. Leyton, C. Mayeur, S.M. Kao, A.E. Pappas, R.T. Peterson, D.B. Bloch, P.B. Yu, M.D. Fleming, K.D. Bloch, Perturbation of hepcidin expression by BMP type I receptor deletion induces iron overload in mice, Blood 118 (2011) 4224–4230, https://doi.org/10.1182/blood-2011-03-339952.
[7] A. Pietrangelo, Genetics, genetic testing, and management of hemochromatosis: 15 years since hepcidin, Gastroenterology 149 (2015) 1240–1251, https://doi.org/10.1053/j.gastro.2015.06.045.
[8] N. Montalbetti, A. Simonin, G. Kovacs, M.A. Hediger, Mammalian iron transporters: families SLC11 and SLC40, Mol. Aspects Med. 34 (2013) 270–287, https://doi.org/10.1016/j.mam.2013.01.002.
[9] A.U. Steinbicker, C. Mayeur, L.K. Lohmeyer, P. Leyton, S.M. Kao, A.E. Pappas, R. Nobre, R.T. Peterson, D.B. Bloch, P.B. Yu, K.D. Bloch, Alk3, a BMP Type I receptor is required for the induction of hepatic hepcidin gene expression by interleukin-6, Blood 123 (2014) 2261–2268, https://doi.org/10.1182/blood-2013-02-480095.K.D.B.
[10] C. Mayeur, P.A. Leyton, S.A. Kolodziej, B. Yu, K.D. Bloch, BMP type II receptors have redundant roles in the regulation of hepatic hepcidin gene expression and iron metabolism, Blood 124 (2014) 2116–2124, https://doi.org/10.1182/blood-2014-04-572644.C.M.
[11] J.S. Becker, M. Zoriy, A. Matusch, B. Wu, D. Salber, C. Palm, J.S. Becker, Bioimaging of metals by laser ablation inductively coupled plasma mass spectrometry (LA-ICP-MS), Mass Spectrom. Rev. 29 (2010) 156–175, https://doi.org/10.1002/mas.20239.
[12] T. Trejos, R. Koons, S. Becker, T. Berman, J. Buscaglia, M. Duecking, T. Eckert-Lumsdon, T. Ernst, C. Hanlon, A. Heydon, K. Mooney, R. Nelson, K. Olsson, C. Palenik, E.C. Pollock, D. Rudell, S. Ryland, A. Tarifa, M. Valadez, P. Weis, J. Almirall, Cross-validation and evaluation of the performance of methods for the elemental analysis of forensic glass by µ-XRF, ICP-MS, and LA-ICP-MS, Anal. Bioanal. Chem. 405 (2013) 5393–5409, https://doi.org/10.1007/s00216-013-6978-y.
[13] T. Trojek, L. Musílek, X-ray fluorescence – a non-destructive tool in investigation of Czech fine and applied art objects, Radiat. Phys. Chem. 137 (2017) 230–233, https://doi.org/10.1016/j.radphyschem.2017.01.007.
[14] N.J. de Winter, M. Sinnesael, C. Makarona, S. Vansteenberge, P. Claeys, Trace element analyses of carbonates using portable and micro-X-ray fluorescence:

performance and optimization of measurement parameters and strategies, J. Anal. At. Spectrom. 32 (2017) 1211–1223, https://doi.org/10.1039/C6JA00361C.
[15] O. Hachmöller, A. Guilherme Buzanich, M. Aichler, M. Radtke, D. Dietrich, K. Schwamborn, L. Lutz, M. Werner, M. Sperling, A. Walch, U. Karst, Elemental bioimaging and speciation analysis for the investigation of Wilson's disease using μXRF and XANES, Metallomics 8 (2016) 648–653, https://doi.org/10.1039/C6MT00001K.
[16] K. Janssens, W. De Nolf, G. Van Der Snickt, L. Vincze, B. Vekemans, R. Terzano, F.E. Brenker, Recent trends in quantitative aspects of microscopic X-ray fluorescence analysis, TrAC Trends Anal. Chem. 29 (2010) 464–478, https://doi.org/10.1016/j.trac.2010.03.003.
[17] D. Guimarães, A.A. Dias, M. Carvalho, M.L. Carvalho, J.P. Santos, F.R. Henriques, F. Curate, S. Pessanha, Quantitative determinations and imaging in different structures of buried human bones from the XVIII-XIXth centuries by energy dispersive X-ray fluorescence – postmortem evaluation, Talanta 155 (2016) 107–115, https://doi.org/10.1016/j.talanta.2016.04.028.
[18] T. Wolff, W. Malzer, I. Mantouvalou, O. Hahn, B. Kanngießer, A new fundamental parameter based calibration procedure for micro X-ray fluorescence spectrometers, Spectrochim. Acta Part B At. Spectrosc. 66 (2011) 170–178, https://doi.org/10.1016/j.sab.2011.01.009.
[19] A.D. Surowka, P. Wrobel, M.M. Marzec, D. Adamek, M. Szczerbowska-Boruchowska, Novel approaches for correction against the soft matrix effects in the quantitative elemental imaging of human substantia nigra tissue using synchrotron X-ray fluorescence, Spectrochim. Acta Part B At. Spectrosc. 123 (2016) 47–58, https://doi.org/10.1016/j.sab.2016.07.014.
[20] R. Sitko, Quantitative X-ray fluorescence analysis of samples of less than "infinite thickness": difficulties and possibilities, Spectrochim. Acta Part B At. Spectrosc. 64 (2009) 1161–1172, https://doi.org/10.1016/j.sab.2009.09.005.
[21] R. Padilla, P. Van Espen, A. Abrahantes, K. Janssens, Semiempirical approach for standardless calibration in μ-XRF spectrometry using capillary lenses, Xray Spectrom. 34 (2005) 19–27, https://doi.org/10.1002/xrs.781.
[22] M.B. Bueno Guerra, C.E.G.R. Schaefer, G.G.A. de Carvalho, P.F. de Souza, D.S. Júnior, L.C. Nunes, F.J. Krug, Evaluation of micro-energy dispersive X-ray fluorescence spectrometry for the analysis of plant materials, J. Anal. At. Spectrom. 28 (2013) 1096–1101, https://doi.org/10.1039/c3ja50084e.
[23] J.S. Becker, A. Matusch, B. Wu, Bioimaging mass spectrometry of trace elements - recent advance and applications of LA-ICP-MS: a review, Anal. Chim. Acta 835 (2014) 1–18, https://doi.org/10.1016/j.aca.2014.04.048.
[24] D.P. Bishop, D. Clases, F. Fryer, E. Williams, S. Wilkins, D.J. Hare, N. Cole, U. Karst, P.A. Doble, Elemental bio-imaging using laser ablation-triple quadrupole-ICP-MS, J. Anal. At. Spectrom. 31 (2016) 197–202, https://doi.org/10.1039/C5JA00293A.
[25] M. Šala, V.S. Šelih, J.T. van Elteren, Gelatin gels as multi-element calibration standards in LA-ICP-MS bioimaging: fabrication of homogeneous standards and microhomogeneity testing, Analyst 142 (2017) 3356–3359, https://doi.org/10.1039/C7AN01361B.
[26] J.-C. Müller, J. Lichtmannegger, H. Zischka, M. Sperling, U. Karst, High spatial resolution LA-ICP-MS demonstrates massive liver copper depletion in Wilson disease rats upon Methanobactin treatment, J. Trace Elem. Med. Biol. 49 (2018) 119–127, https://doi.org/10.1016/j.jtemb.2018.05.009.
[27] C. Postic, M. Shiota, K.D. Niswender, T.L. Jetton, Y. Chen, J.M. Moates, K.D. Shelton, J. Lindner, A.D. Cherrington, M.A. Magnuson, Dual roles for glucokinase in glucose homeostasis as determined by lver and pancreatic b cell-specific gene knock-outs using crer recombinase, J. Biol. Chem. 274 (1999) 305–315, https://doi.org/10.1074/jbc.274.1.305.
[28] B. Sauer, Functional expression of the cre-lox site-specific recombination system in the yeast Saccharomyces cerevisiae, Mol. Ans Cell. Biol. 7 (1987) 2087–2096, https://doi.org/10.1128/MCB.7.6.2087.Updated.
[29] Y. Mishina, M.C. Hanks, S. Miura, M.D. Tallquist, R.R. Behringer, Generation of Bmpr/Alk3 conditional knockout mice, Genesis 32 (2002) 69–72, https://doi.org/10.1002/gene.10038.
[30] J.D. Torrance, T.H. Bothwell, Tissue iron stores, in: J.D. Cook (Ed.), Iron. Methods Hematol. Vol. 1 Churchill Livingstone, New York, 1981, pp. 90–115.
[31] L. Traeger, I. Gallitz, R. Sekhri, N. Bäumer, T. Kuhlmann, C. Kemming, M. Holtkamp, J.-C. Müller, U. Karst, F. Canonne-Hergaux, M.U. Muckenthaler, D.B. Bloch, A. Olschewski, T.B. Bartnikas, A.U. Steinbicker, ALK3 undergoes ligand-independent homodimerization and BMP-induced heterodimerization with ALK2, Free Radic. Biol. Med. 129 (2018), https://doi.org/10.1016/j.freeradbiomed.2018.09.021.
[32] D. Brune, G. Nordberg, P.O. Wester, Distribution of 23 elements in the kidney, liver and lungs of workers from a smeltery and refinery in north Sweden exposed to a number of elements and of a control group, Sci. Total Environ. 16 (1980) 13–35, https://doi.org/10.1016/0048-9697(80)90100-X.
[33] P.W.J.M. Boumans, Measuring detection limits in inductively coupled plasma emission spectrometry using the "SBR—RSDB approach"—I. A tutorial discussion of the theory, Spectrochim, Acta Part B At. Spectrosc. 46 (1991) 431–445, https://doi.org/10.1016/0584-8547(91)80040-A.
[34] T.W. May, R.H. Wiedmeyer, A table of polyatomic interferences in ICP-MS, At. Spectrosc. 19 (1998) 150–155.
[35] K. Bischoff, S.K. Ramaiah, Liver toxicity, in: R.C. Gupta (Ed.), Vet. Toxicol. Basic Clin. Princ. Elsevier Inc., 2007, pp. 154–160, , https://doi.org/10.1016/B978-0-12-370467-2.50107-3.
[36] S. Zumerle, J.R.R. Mathieu, S. Delga, M. Heinis, L. Viatte, S. Vaulont, C. Peyssonnaux, Targeted disruption of hepcidin in the liver recapitulates the hemochromatotic phenotype, Blood 123 (2014) 3646–3650, https://doi.org/10.1182/blood-2014-01-550467.